# SUPPLEMENTARY INFORMATION

## Topological Path-Connectivity and Diffusion

Yohannes Abate[1,*], Michael Usher[2], Maninder Kaur[1,3], Andre Erpenbeck[1,3], Miyuki Karunathilaka[1], Mason Caron[1], Sarabpreet Singh[1]

[1]Department of Physics and Astronomy, University of Georgia, Athens, Georgia, USA
[2]Department of Mathematics, University of Georgia, Athens, Georgia, USA
[3]Center for Simulational Physics, University of Georgia, Athens, Georgia, USA

[*]Yohannes.Abate@uga.edu

December 31, 2025

## 1 Monte Carlo Simulation

Fig. S1 presents additional trajectory visualizations for the corridor geometry in which the absorbing target is located in the right subregion. Panels (a) and (b) show five representative trajectories each for neck widths $w = 80$ and $w = 50$, respectively, illustrating how trajectories traverse increasingly constrained passages.

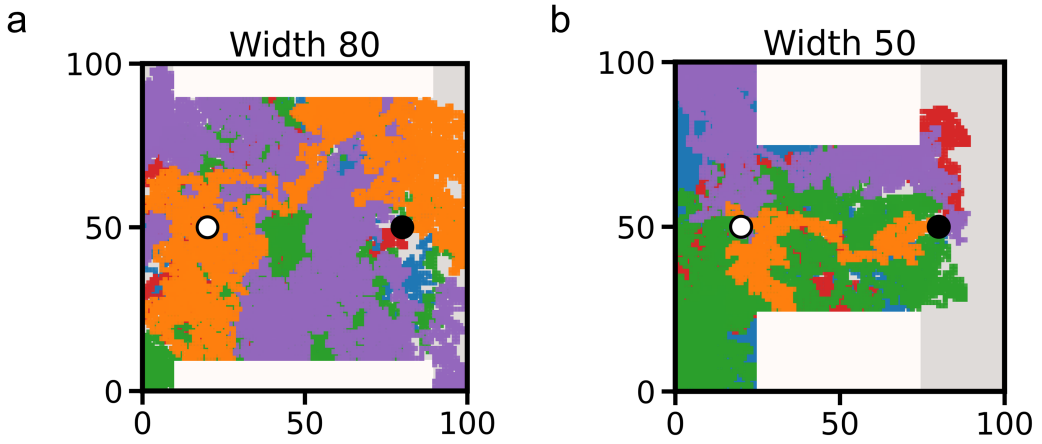


**Figure S1.** Controlled deformation and connectedness for target in right subregion. (a) Sample trajectories for neck width $w = 80$. (b) Sample trajectories for neck width $w = 50$. Five trajectories are shown in each panel.

Fig. S2 shows the corresponding results for the configuration in which the target lies inside the constriction. Panel (a) provides representative trajectories for neck widths $w = 100$ down to $w = 10$. Panels (b)–(e) summarize the smoothed arrival-time distributions, MFPTs with standard-error bars, and arrival-time histograms on linear, semi-log, and log–log axes. Fig. S3 reports boundary-contact statistics for all three domain families. For each geometry, we separate successful trajectories into two categories: those that contacted the boundary at least once and those that reached the target without touching the boundary. Panel (a) shows results for the five equal-area deformed shapes *i*–*v*. Panel (b) presents the same analysis for the corridor geometries with the target in the right subregion, and panel (c) for the corridor geometries with the target at the center of the constriction. All statistics are based on $N = 2000$ successful trajectories per geometry.

## 2 Finite Element Simulation for a Target within the Constriction

This section complements the analysis presented in Sec.3.2.2 of the main text. In Fig. S4, we investigate diffusion in a two-dimensional square domain of unit length that becomes progressively constricted at its center, with the target located inside the constricted region. Panels (a)–(h) show results for increasing constriction strength. In the weakly constricted regime (panels (a)–(d)), the mean first-arrival time remains nearly unchanged, as indicated by the predominantly yellow and green color maps and by the concentric contour lines centered on the target. The influence of the constriction and the domain boundaries is limited to the periphery, demonstrating that diffusion is remarkably robust to moderate geometric deformations. When the constriction becomes more pronounced (panels (e)–(h)), the behavior changes qualitatively. The mean arrival times increase substantially, reflected by a shift toward orange and red colors, indicating that the particles require significantly more time to reach the target. In addition, distinct vertical contour lines appear within the constriction, signifying directed vertical diffusion, while circular contours form around the entrances of the constriction, indicating that the process of entering the narrow region now dominates the overall arrival dynamics.

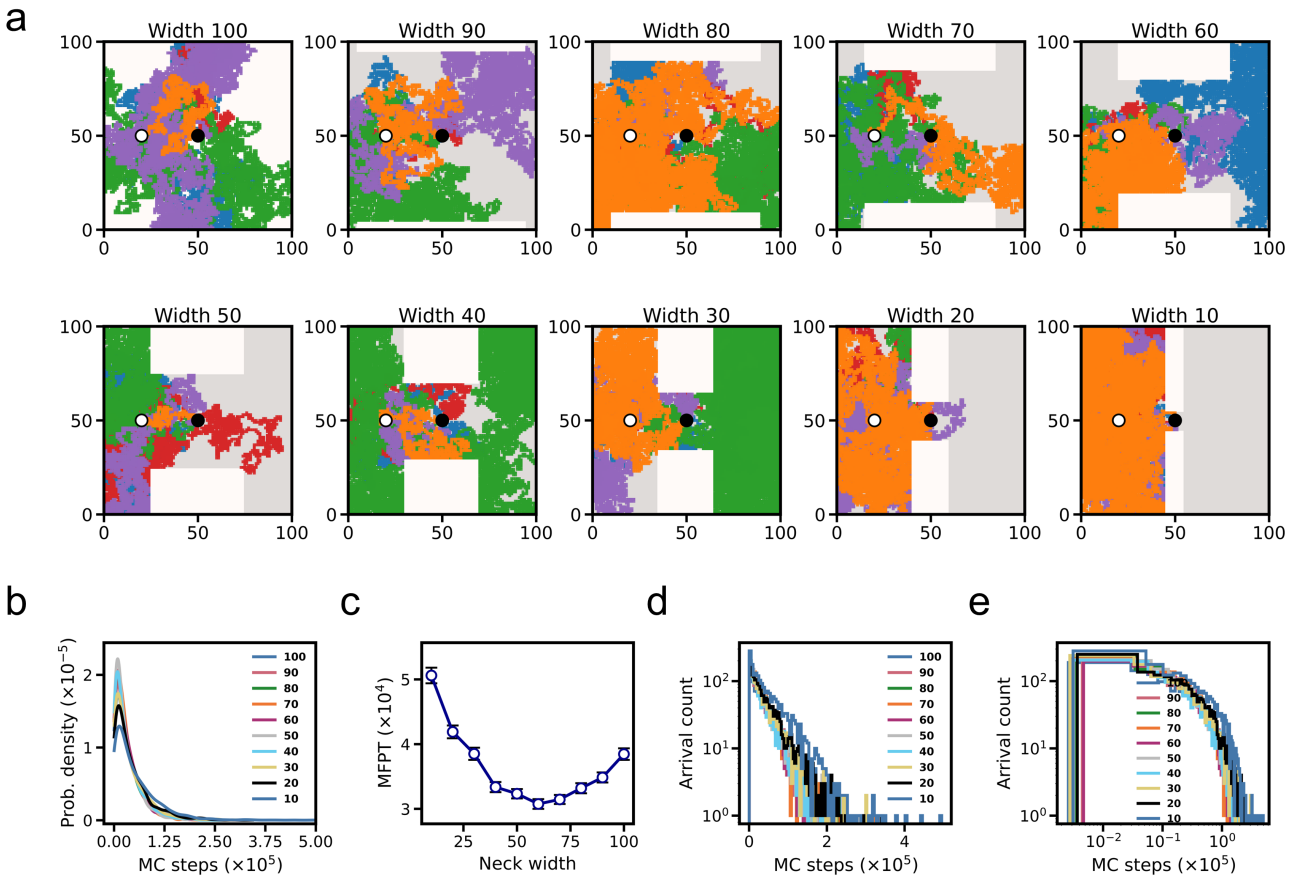


**Figure S2.** Controlled deformation and connectedness for target within corridor. (a) Sample trajectories for neck widths $w = 100 \rightarrow 10$ (five trajectories each). (b) Smoothed arrival-time distributions for each $w$. (c) MFPT versus neck width with SEM error bars. (d–e) Arrival-time histograms on semi-log and log–log scales. In (b), particle counts are normalized to form a smooth arrival-time probability density, whereas (d) and (e) display the same arrival-time data as unnormalized particle counts to probe possible scaling behavior (exponential versus power-law).

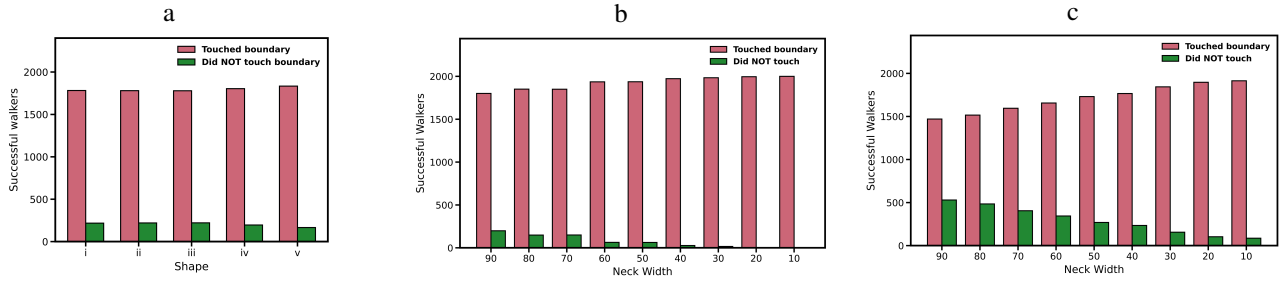


**Figure S3.** Boundary-contact statistics for the three domain families. (a) Number of successful trajectories that touched the outer boundary (pink) and those that reached the target without touching the boundary (green) for the five equal-area deformed shapes *i*–*v* shown in Fig.2. (b) Corresponding counts for corridor geometries with the target placed in the right subregion, for neck widths $w = 90$ to $w = 10$, corresponding to the domains shown in Fig.3. (c) Same analysis for corridor geometries with the target placed at the center of the corridor, corresponding to the domains shown in Fig. S2. All results are based on $N = 2000$ successful trajectories per geometry.

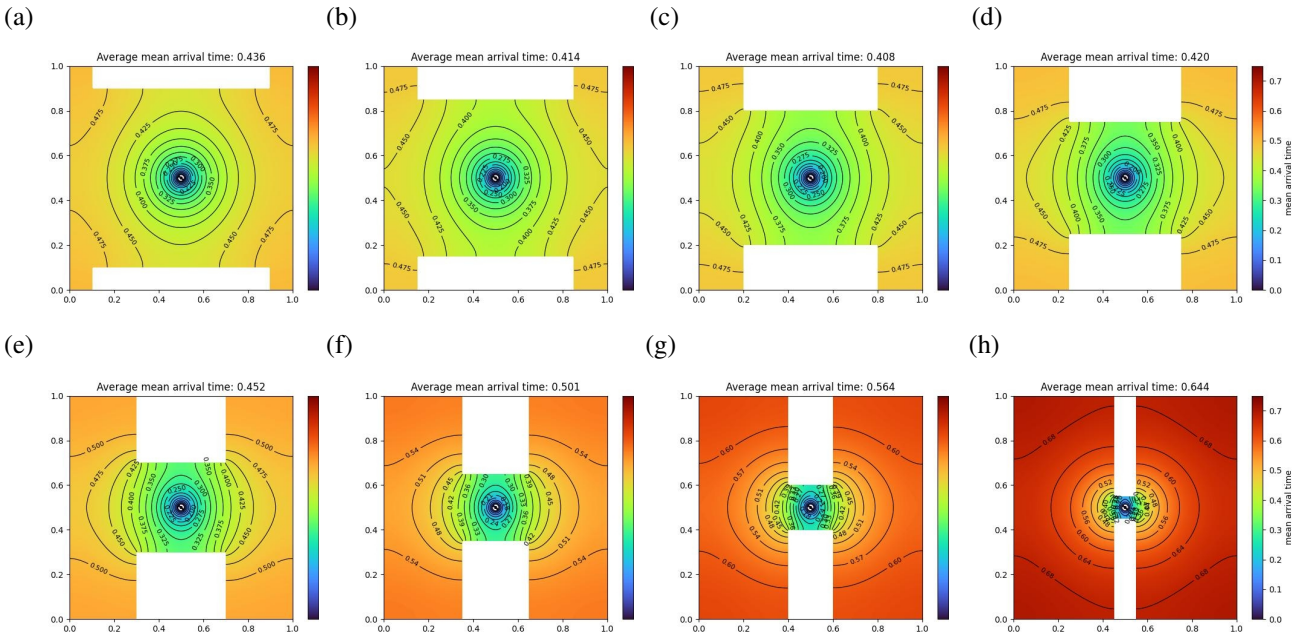


**Figure S4.** Diffusion toward a target within a constriction. The colormap shows the mean first-arrival times for increasing constriction strength in panels (a)–(h). The contour lines highlight the influence of the geometry and the constriction on the overall diffusive behavior. All results were obtained by numerically solving the Poisson equation. For small to intermediate constrictions in panels (a)–(d), diffusion remains nearly isotropic and robust to deformation. Strong constrictions as in panels (e)–(h) lead to delayed arrival times and the emergence of vertical and circular contour features around the constriction that mark diffusion processes limited by entry into the constriction.

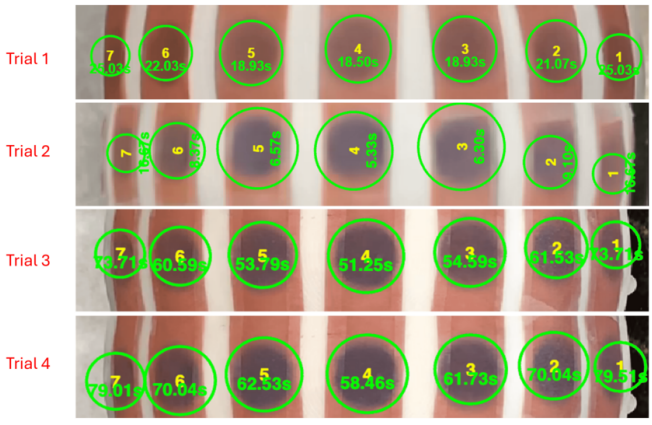


**Figure S5.** Final litmus-paper frames used for FPT extraction across four trials. Each ROI shows the measured FPT obtained by tracking the normalized blueness field $C_b = \dfrac{B}{R+G+B+\varepsilon}$ and detecting when $C_b(t)$ exceeded 20% of its dynamic range. Green-outlined ROIs indicate threshold crossings, allowing direct comparison of transition timing and contour-level coherence among trials.

| Time Difference Calculation | Contour 1 (ROI 5 & ROI 3) | Contour 2 (ROI 6 & ROI 2) | Contour 3 (ROI 7 & ROI 1) |
|---|---|---|---|
| Trial 1 | 0.00 s | 0.96 s | 0.00 s |
| Trial 2 | 0.20 s | 0.73 s | 0.00 s |
| Trial 3 | 0.80 s | 0.94 s | 0.00 s |
| Trial 4 | 0.80 s | 0.00 s | 0.50 s |

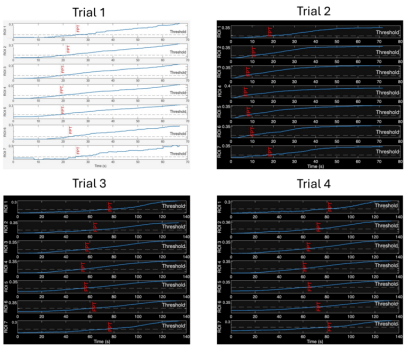


**Figure S6.** Left: Time differences between paired ROIs along each contour across all trials. Measured first-passage-time (FPT) differences between the two openings on each contour of the 3D-printed hemisphere show variations consistently below 1 s across four repeated experiments. These small offsets likely arise from minor differences in litmus-paper wetness, local humidity, or lighting fluctuations, and confirm that ammonia diffusion along each contour occurs nearly simultaneously, demonstrating high spatial symmetry and reproducibility of the gas-propagation process. Right: Blueness time-series curves for all ROIs across four independent trials. Temporal evolution of the normalized blueness signal $C_b(t)$ is shown for each ROI, with solid blue curves indicating the measured trajectories and dashed horizontal lines marking the 20% dynamic-range threshold used to define FPTs. Red vertical markers denote the frame at which each ROI first exceeds and sustains this threshold. Across trials, the blueness evolution exhibits smooth, coherent transitions with minimal temporal discontinuity between paired ROIs in the same contour, confirming stable nd reproducible ammonia diffusion dynamics throughout the hemisphere model.

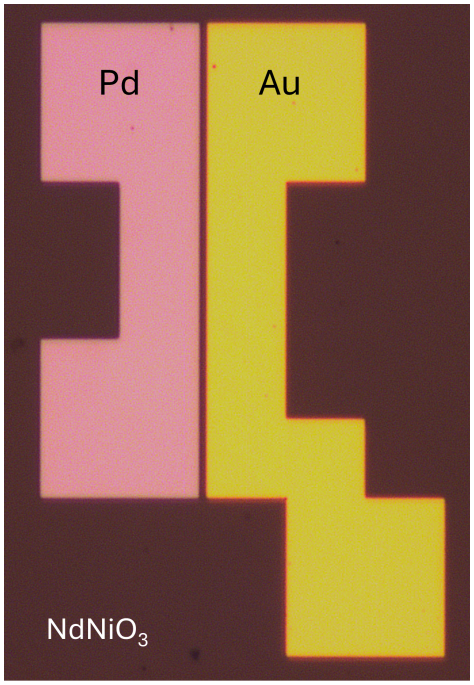


**Figure S7.** An optical microscope image showing the device structure fabricated on an $NdNiO_3$ thin film. The image features two distinct metal contact pads: a Palladium (Pd) pad on the left and a Gold (Au) pad on the right, separated by a narrow channel.

**VIDEOS**

(Gas phase SI video 1)

Raw Liquid Phase SI Video 1

Heat Map Liquid Phase SI Video 2